

# Fault identification for buried strike-slip earthquakes using InSAR: The 1994 and 2004 Al Hoceima, Morocco earthquakes

Juliet Biggs,<sup>1</sup> Eric Bergman,<sup>2</sup> Brian Emmerson,<sup>3</sup> Gareth J. Funning,<sup>4</sup> James Jackson,<sup>3</sup> Barry Parsons<sup>1</sup> and Tim J. Wright<sup>1</sup>

<sup>1</sup>COMET, Department of Earth Sciences, University of Oxford. E-mail: julietb@earth.ox.ac.uk

<sup>2</sup>CIEI, Department of Physics, University of Colorado, Boulder, Colorado, 80309, USA

<sup>3</sup>COMET, Bullard Laboratories, Department of Earth Sciences, University of Cambridge

<sup>4</sup>Berkeley Seismological Laboratory, University of California, Berkeley, California, USA

Accepted 2006 May 15. Received 2006 May 15; in original form 2005 September 15

## SUMMARY

The 1994  $M_w$  6.0 and 2004  $M_w$  6.5 Al Hoceima earthquakes are the largest to have occurred in Morocco for 100 yr, and give valuable insight into the poorly understood tectonics of the area. Bodywave modelling indicates the earthquakes occurred on near-vertical, strike-slip faults with the nodal planes oriented NW–SE and NE–SW. Distinguishing between the primary fault plane and auxiliary planes, using either geodetic or seismic data, is difficult due to the spatial symmetry in deformation fields and radiation pattern of moderately sized, buried, strike-slip earthquakes. Preliminary studies, using aftershock locations and surface observations, have been unable to identify the orientation of the primary fault plane for either earthquake conclusively. We use radar interferometry and aftershock relocation of the earthquake sequence to resolve the ambiguity.

For the 2004 earthquake, inverting the interferograms for a uniform slip model based either of the two potential nodal planes results in similar misfits to the data. However, the NE–SW best-fit fault plane has an unrealistically high fault slip-to-length ratio and we conclude the NW–SE striking nodal plane is the primary fault plane and slip was right lateral. We carry out tests on synthetic data for a buried strike-slip earthquake in which the orientation of the fault plane is known a priori. Independent of geometry, missing data, and correlated noise, models produced assuming the auxiliary plane to be the fault plane have very high fault slip-to-length ratios. The 1994 earthquake had a smaller magnitude and comparisons of model misfits and slip-to-length ratios do not conclusively indicate which of the nodal planes is the primary fault plane. Nonetheless, the InSAR data provides valuable information by improving the accuracy of the earthquake location by an order of magnitude.

We carry out a multiple event relocation of the entire earthquake sequence, including aftershocks, making use of the absolute locations for the 1994 and 2004 main shocks from our InSAR study. The aftershock locations are consistent with a NW–SE orientated fault plane in 2004 and suggests that the 1994 earthquake occurred on a NE–SW fault; perpendicular to the fault which ruptured in 2004. Previous tectonic models of the area proposed a bookshelf model of block rotation with NNE–SSW left-lateral faults. This model requires modification to accommodate the observation of right-lateral slip on a NW–SE fault plane for the 2004 earthquake and we prefer to interpret the fault orientations as due to a zone of distributed shear with a right-lateral fault striking at  $\sim 115^\circ$  and conjugate, clockwise rotating, left-lateral faults striking at  $\sim 25^\circ$ .

**Key words:** aftershocks, continental deformation, earthquake source mechanisms, fault model, satellite geodesy, waveform analysis.

## 1 INTRODUCTION

Two large earthquakes have occurred in the Al Hoceima Region of Morocco in the past 11 yr. On May 26 1994, a  $M_w$  6.0 earthquake caused significant damage and two deaths. On February 24 2004,

a  $M_w$  6.5 earthquake caused over 600 fatalities with 40 000 made homeless. These earthquakes are the largest to have occurred in Morocco for 100 yr, and give valuable insight into the poorly understood tectonics of this area. Preliminary catalogued solutions (e.g. Harvard Centroid Moment Tensor) for both earthquakes show

**Table 1.** Published source parameters for the 1994 and 2004 Al Hoceima earthquakes, determined using the seismological technique listed in the first column. Strikes, dips and rakes of the two nodal planes are s1, d1, r1 and s2, d2, and r2, and z is the determined centroid depth, where available. Nodal planes from moment tensor inversions correspond to the best double couple solution and asterisks (\*) denote depths that were fixed in the inversion. Linear vector dipole components ( $\epsilon$ ) for the Harvard and USGS moment tensor solutions are calculated using the definition of Julian *et al.* (1998). Bezzeghoud & Buforn (1999) waveform-modelled the 1994 earthquake as two subevents, with the first ( $M_w$  5.3) event having a mechanism that matches the first motion solution from the same study, and the second ( $M_w$  5.7) having the mechanism listed here. The moment magnitude ( $M_w$ ) is flagged 'm' for this entry, and is calculated from the cumulative moment released by both events. The various source parameters listed here are compared in Figs 3 and 5.

Method	s1	d1	r1	s2	d2	r2	z/km	$\epsilon$	$M_w$	Focal sphere	Source publication
1994 earthquake											
Moment tensor inversion	17	85	-42	112	48	-173	*15	0.30	5.9		Harvard CMT (Dziewonski <i>et al.</i> 1981)
	2	84	-10	93	80	-174	19	-0.01	5.9		USGS (Sipkin 1982, 1986a,b)
First motions	202	60	23	100	72	145	.	.	.		El Alami <i>et al.</i> (1998)
	330	77	-45	73	46	-162	.	.	.		Bezzeghoud & Buforn (1999)
Waveform modelling	355	69	2	264	88	159	7	.	5.8m		Bezzeghoud & Buforn (1999)
	117	81	-175	26	85	-9	8	.	5.9		This study
2004 earthquake											
Moment tensor inversion	113	61	-170	18	81	-29	*12	0.24	6.3		Harvard CMT (Dziewonski <i>et al.</i> 1981)
	111	89	-176	21	86	-1	13	0.08	6.4		USGS (Sipkin 1982, 1986a,b)
	106	74	-161	11	72	-17	14	0.04	6.3		Stich <i>et al.</i> (2005)
Waveform modelling	298	83	179	28	89	7	6	.	6.4		This study

strike-slip mechanisms with nodal planes striking at  $\sim 20^\circ$  (left lateral) and  $\sim 290^\circ$  (right lateral) (Table 1).

### 1.1 Tectonic background

The Alboran Region, an oblique collision zone between the Nubian and Eurasian Plates, marks the western extent of the Alpine oro-

genic belt (Fig. 1). Using the pole of rotation determined from GPS data (McClusky *et al.* 2003), the present-day convergence rate is  $5.5 \text{ mm yr}^{-1}$  in a WNW-ESE orientation. Geological estimates of plate motion based on seafloor spreading rates and transform fault azimuths place the pole of rotation much further south than the geodetic estimates, indicating the pole of rotation may have migrated northwards in the last 3 Ma (Calais *et al.* 2003).

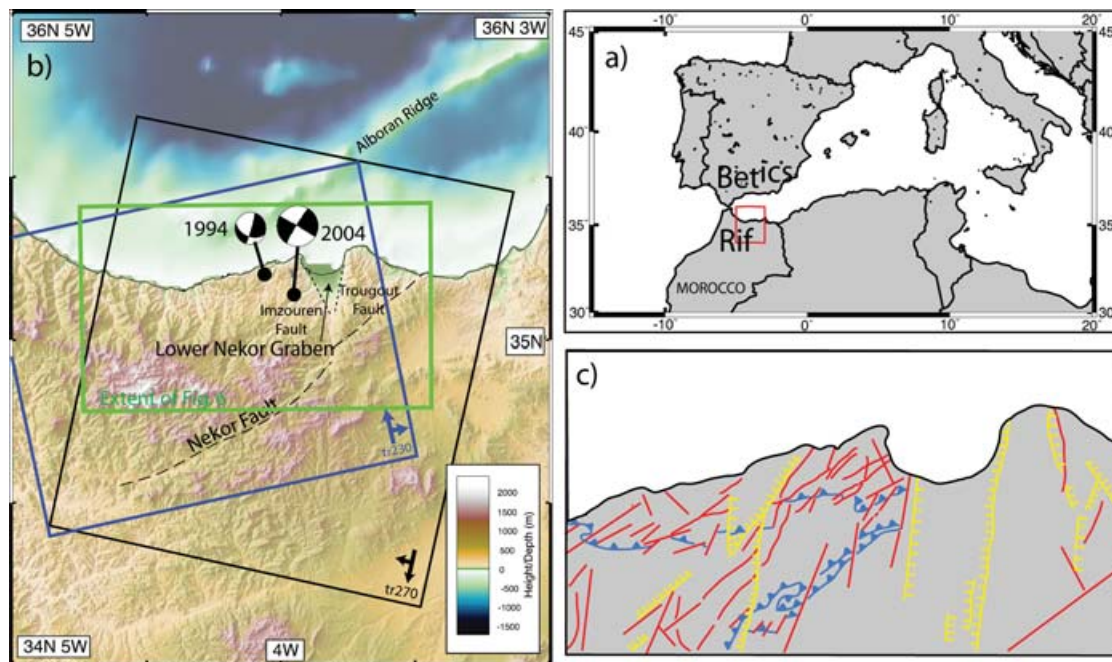


**Figure 1.** (a) Location of the Al Hoceima Region of Morocco. (b) Topography and major tectonic features of the Al Hoceima Region of Morocco. Location of the ascending (tr 230) and descending (tr 270) satellite tracks are also shown. Long arrows are direction of satellite travel and short arrows are the satellite look direction. Focal mechanisms and earthquake locations are taken from this study. The Jebha Fault is located west of this region. (c) Map showing previously identified structural trends red-fault; yellow-normal fault; blue-thrust (modified from Ait Brahim *et al.* 1990).

The Al Hoceima Region is situated on the Mediterranean Coast of Morocco, at the junction between the Rif Mountain Belt and the offshore Alboran Ridge. The Moroccan Rif is part of a highly arcuate thrust belt which extends to the Betic Mountains in southern Spain. The area has a complex tectonic history and as a result is highly fractured with numerous structural trends (Fig. 1c). The principal geological structures are a series of N–S horsts and grabens and two parallel left-lateral strike-slip faults, the Nekor and Jebha Faults. The region is also fractured by a series of NE–SW to N–S striking high angle faults with left-lateral offsets and a set of minor, conjugate faults orientated NW–SE with apparent right lateral offsets (Calvert *et al.* 1997; Ait Brahim *et al.* 1990).

The most significant of the N–S grabens is the Lower Nekor graben, bounded by the NNW–SSE Imzouren and N–S Trougout Faults and filled with 400–500 m of Quaternary alluvial deposits (Ait Brahim *et al.* 1990; Meghraoui *et al.* 1996). The normal faults, which are segmented on a 20 km lengthscale, are clearly visible at the surface as escarpments with exposed fault planes, suggesting recent activity (Meghraoui *et al.* 1996). Indeed, the majority of the region's microseismicity is located inside the Lower Nekor graben and displays strike-slip or normal faulting mechanisms (Hatzfeld *et al.* 1993).

The Nekor fault is the main geomorphological feature in the region and has a reported left-lateral geological offset of ~50 km (Leblanc & Olivier 1984). The NE–SW orientation of Nekor and Jebha strike-slip faults is parallel to the direction of thrust sheet transport within the Rif Mountains. However, further west, similarly orientated structures coincides with an ocean-continent transition zone offshore and a normal-thickness to thinned continental crust transition onshore. As a result there is some debate over whether the structures formed during the main Rif orogeny or are the result of an underlying structural trend inherited from the passive margin of Africa (Morley 1987). Studies of microseismicity have found no evidence of current activity on the Nekor Fault (Hatzfeld *et al.* 1993) and, although these faults may have been important structures during the Miocene, present-day strain is likely to be accommodated on alternative structures, including the N–S system of horsts and grabens (Ait Brahim *et al.* 1990).

Previous authors have interpreted the Al Hoceima area as region of distributed right-lateral shear with crustal blocks orientated NNE–SSW rotating clockwise, which results in left-lateral strike-slip motion on their boundaries (e.g. Dillon *et al.* 1980; Meghraoui *et al.* 1996; Calvert *et al.* 1997).

## 1.2 Previous observations of the 1994 and 2004 earthquakes

For most earthquakes of medium–large magnitude, the fault plane and auxiliary planes can be distinguished using surface faulting, aftershock relocation and/or structural trends. Aftershock locations for the 1994 earthquake were studied using data from the Moroccan regional network (Calvert *et al.* 1997) and a temporary network (El Alami *et al.* 1998). Both studies found a NNE–SSW trending cluster, 30 km long and 10 km wide and, therefore, concluded the earthquake occurred on a fault orientated NNE–SSW. However, the NNE–SSW trending cluster of El Alami *et al.* (1998) is only seen for aftershocks  $\leq 3$  km deep, which may represent processes in the upper weaker layers of the crust rather than the fault plane at depth. When aftershocks at all depths are considered there is no trend to the aftershock locations. The majority of stations in the Moroccan regional network used by Calvert *et al.* (1997) are lo-

calated to the south of the earthquake. There is, therefore, an average azimuthal gap in station coverage of 200°. Consequently, the direction of maximum epicentral uncertainty also trends NNE–SSW and it is unclear whether this trend is real, or an artefact of the station distribution.

Following the 2004 Al Hoceima earthquake, tensile en-echelon and sigmoidal cracks orientated NE–SW to NNE–SSW were observed, leading some researchers (e.g. Ait Brahim *et al.* 2004; Stich *et al.* 2005) to conclude that the earthquake occurred on a left-lateral strike-slip fault orientated NNE–SSW to NE–SW. No significant surface ruptures were reported. More than 500 aftershocks with  $M \geq 2.3$  were recorded in the two weeks following the main shock, but preliminary aftershock locations appear as a diffuse cloud over a 20 by 20 km area with no clear trend (Cherkaoui & Harnafi 2004). Since these observations are unable to unambiguously distinguish between the primary fault plane and the auxiliary plane for either earthquake, we use remotely sensed geodetic data and multiple event relocation of the aftershocks to try to resolve this ambiguity.

## 2 SEISMOLOGICAL DETERMINATION OF SOURCE GEOMETRY

In order to provide better constraints on the source mechanisms for the 1994 and 2004 Al Hoceima earthquakes, we model teleseismic long-period waveforms. The method is summarized here, and is described in more detail elsewhere (e.g. Nabelek 1984; Molnar & Lyon-Caen 1989; Maggi *et al.* 2000). Using broad-band seismograms from the Global Digital Seismograph Network (GDSN) and a deconvolution procedure to change the response to that of a WWSSN 15–100 s long-period instrument, we invert the resulting  $P$  and  $SH$  waveform data for the source time function, scalar moment, strike, dip, rake, and centroid depth. Constraining the source to be a pure double-couple, we then use the MT5 version (Zwicky *et al.* 1994) of the algorithm developed by McCaffrey & Abers (1988) and McCaffrey *et al.* (1991) to model  $P$ ,  $pP$  and  $sP$  phases on vertical component seismograms in the epicentral distance range 30–90°, and  $S$  and  $sS$  phases on transverse components in the range 30–80°. Amplitudes are corrected for geometrical spreading, and for anelastic attenuation using Futterman operators with a  $t^*$  of 1.0 and 4.0 s for  $P$  and  $SH$  waves respectively. We use a simple half-space source velocity model, with  $V_p = 5.9$  km s<sup>-1</sup>,  $V_s = 3.4$  km s<sup>-1</sup>, and density  $\rho = 2800$  kg m<sup>-3</sup>, corresponding to Lamé elastic constants  $\mu = \lambda = 3.23 \times 10^{10}$  Pa.

### 2.1 Seismological observations of the 1994 earthquake

Numerous focal mechanisms have been proposed for the 1994 Al Hoceima earthquake, all showing strike-slip motion with either reverse or normal components (Table 1). Our best-fitting ('minimum misfit') fault plane solution has either right-lateral slip on a fault striking 117° ESE, or left-lateral slip on a fault striking 26° NNE (Figs 2 and 3a). Both nodal planes are near vertical. Formally, the best fit is achieved using a centroid depth of 8 km, though neither the fit to the seismograms nor the best-fitting source orientation are severely altered for depths between 4 and 12 km.

Our minimum misfit solution provides a much better fit to the  $SH$  waves than to the  $P$  waves. This is not unusual for strike-slip events since, at stations close to the nodal planes,  $P$  waves generally have lower signal-to-noise than  $SH$ , and are very sensitive to velocity structure and the precise orientation of the nodal planes.

## 1994 May 26, Al Hoceima

117 / 81 / -175 / 8 / 7.1e17

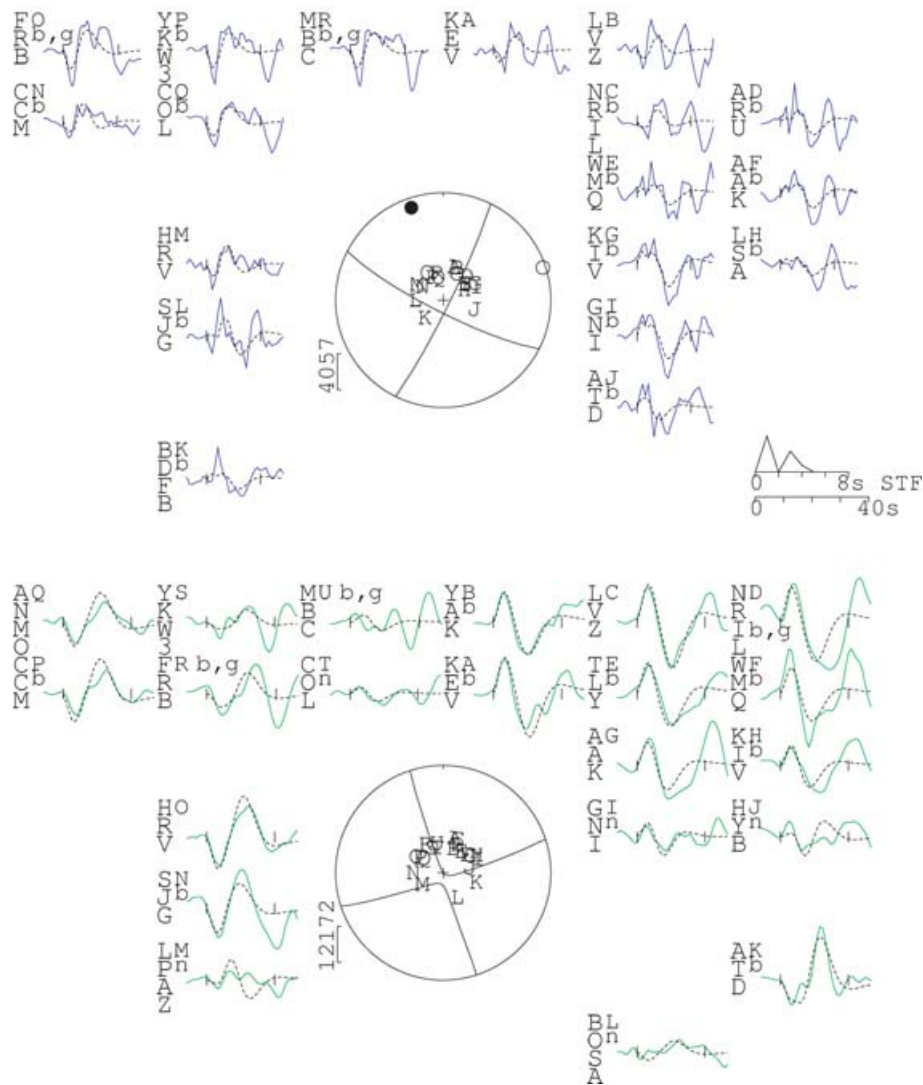


**Figure 2.** Vertical (top) and transverse (bottom) component waveforms for the 1994 Al Hoceima earthquake. Here, we present our best fitting ('minimum misfit') solution determined from waveform inversion, with strike  $117^\circ$ , dip  $81^\circ$ , rake  $-175^\circ$ , depth 8 km, and scalar moment  $7.1 \times 10^{17}$  Nm ( $M_w$  5.9). By modelling the  $P$ ,  $pP$ , and  $sP$  phases on the vertical component, and the  $S$  and  $sS$  phases on the transverse component, synthetic waveforms (dashed lines) were fitted to the observed ones (solid lines) at each station in the window delimited by two vertical bars. The horizontal timescale for both sets of waveforms is shown to the lower right of the  $P$  focal sphere, along with the source time function (STF), which is parametrized by a series of overlapping isosceles triangles. Vertical bars and numbers beside each focal sphere denote amplitudes (in  $\mu\text{m}$ ) of the plotted seismograms. Each waveform is labelled by its station code and an additional capital letter. The capital letters are ordered clockwise by azimuth and correspond to the event-station ray-path's intersection with the lower hemisphere. Lowercase letters by each station provide additional information about waveform alignments and amplitudes. A lowercase  $b$  indicates that the long-period synthetic waveform was aligned with an arrival picked from the original broad-band record; all other records were aligned by eye once sufficiently accurate synthetics were produced. Stations that were difficult to realign because of their nodal character are labelled  $n$ , and were not included in the inversion; records for which we have made adjustments to the station gain are marked by a lowercase  $g$  and were not included in the inversion either. As such, of the 18  $P$  and 21  $SH$  waveforms presented here, 16  $P$  and 13  $SH$  were used in the inversion.

Although a dip-slip solution (Fig. 3b) produces approximately the same  $SH$  nodal surfaces as the predominantly strike-slip minimum misfit mechanism, the shapes and, more significantly, the relative amplitudes of the synthetic  $P$  and  $SH$  waveforms do not match those seen in the data. Because there is often a significant trade-off between centroid depth and source time function duration (particularly for source time functions comprising two distinct pulses, as for our best-fitting solution) we test the effect of restricting the source

time function to a single triangular element of 1 s half duration, and allow all other parameters to vary in the inversion (Fig. 3c). Neither the resulting modelled source parameters nor the fit to the data were significantly altered, indicating that the modelled double pulse in the minimum misfit source time function may not provide an accurate representation of the rupture history. As expected, the inversion converges on a slightly deeper centroid depth (9 km) in an attempt to fit the width of the observed seismograms.

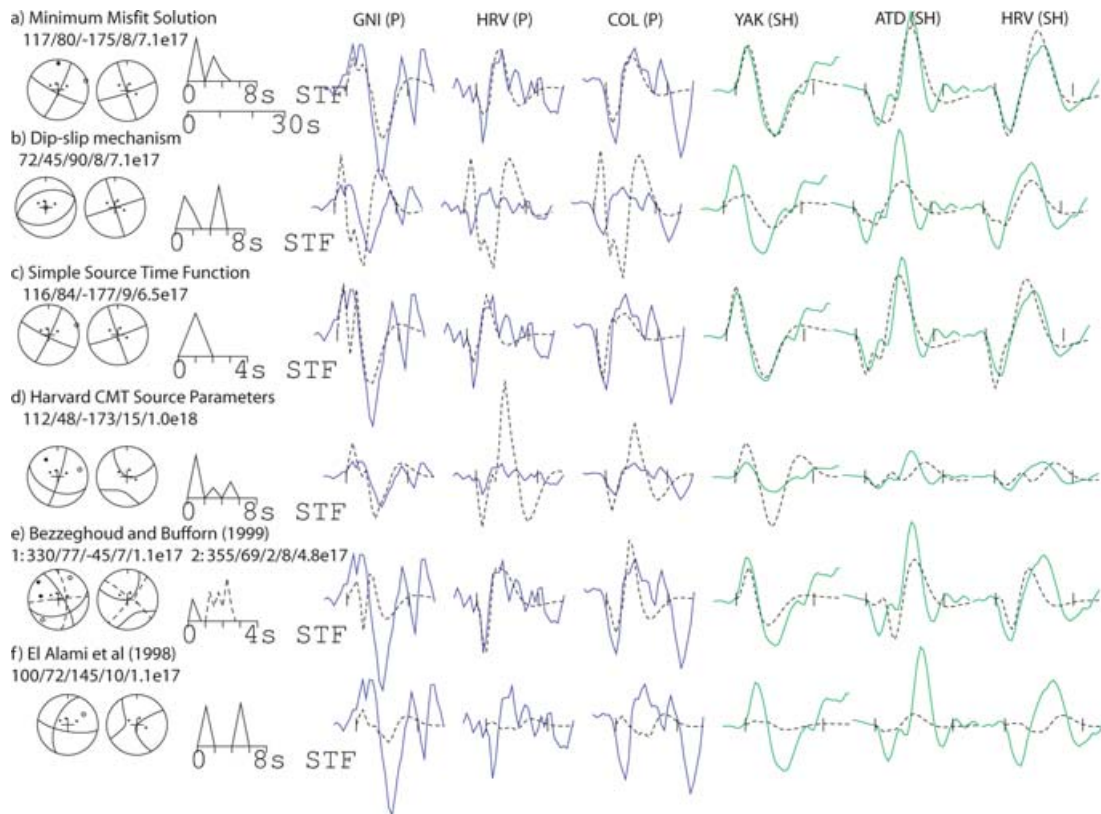


**Figure 3.** Comparison of published solutions for the 1994 Al Hoceima earthquake (Table 1). Three vertical (*P*) and three horizontal (*SH*) component waveforms from Fig. 2 are displayed for each modelled solution, with dots indicating the station positions in their respective focal spheres, shown left. The modelled strike, dip, rake, depth (in km), and scalar moment (in N m) are listed above each pair of focal spheres. (a) The minimum misfit solution shown in Fig. 2. (b) Dip-slip mechanism. This produces approximately the same *SH* nodal surfaces as the predominantly strike-slip minimum misfit mechanism (a). The shapes and the relative amplitudes of the synthetic *P* and *SH* waveforms do not match those seen in the data. [In this line, the *P* waveforms are plotted at  $\frac{1}{2}$  the magnification of line a]. (c) Simple Source Time Function. Neither the resulting modelled source parameters nor the fit to the data were significantly affected but the inversion converged on a slightly deeper centroid depth (10 km). (d) Harvard CMT source parameters (as in Table 1). Synthetic seismograms were produced with the best-fitting source time function and are plotted at  $\frac{1}{3}$  the magnification of line a. The seismogram amplitudes are overestimated. (e) Bezzeghoud & Buffon (1999) The double-source solution modelled by Bezzeghoud & Buffon (1999) using eight broad-band *P* waveforms (f) First motion solution of El Alami *et al.* (1998). The source time function and moment were free to vary in the inversion and the centroid depth was fixed at 10 km. The models d–f do not provide as good a fit to the long period data as our best fitting model (a).

In Figs 3(d)–(f), we compare our model with previously published results. The Harvard CMT source parameters (as in Table 1), are modelled using the source time function that best fits the data. The fit to the waveform shapes is clearly degraded, and the scalar moment of  $1.0 \times 10^{18}$  N m overestimates the observed seismogram amplitudes (Fig. 3d). Although Bezzeghoud & Buffon (1999) waveform-modelled broad-band data for this event using the same algorithm as we do here, their solution uses just eight *P* waveforms and did not use *SH* records. We have used 16 *P* and 13 *SH* waveforms in our inversion for all source parameters, and are able to compare our results with a further two *P* and eight *SH* records (all shown in Fig. 2). For the majority of both vertical and transverse component waveforms, we align the long-period synthetics with arrivals picked from the original broad-band data. The solution of Bezzeghoud & Buffon (1999) does not provide as good a fit to the long-period data as our minimum misfit solution (Fig. 3e). We model the first motion solution of El Alami *et al.* (1998, Table 1), with the source time function and moment free to vary in the inversion and the centroid depth fixed at 10 km. The source time function separates into two well-separated pulses in an attempt to fit the data and this source orientation produces a poor fit to the long-period waveforms (Fig. 3f).

## 2.2 Seismological Observations of the 2004 earthquake

The best-fitting solution for the 2004 earthquake shows either a right-lateral strike-slip fault with a strike of  $298^\circ$  NNW or left-lateral strike-slip with a strike of  $28^\circ$  NNE (Figs 4 and 5a). As with the 1994 event, both nodal planes are near vertical and the fit to the observed seismograms is significantly better for the *SH* records than for the *P* ones. The centroid depth can take values between 2 and 9 km without seriously affecting the fit to the observed seismograms, and there is a significant trade-off between centroid depth and dip for the NW nodal plane. The dip of this plane varies between  $68^\circ$  for a centroid 3 km deep, and  $86^\circ$  for a centroid 10 km deep. Again, we test the trade-off between centroid depth and source time function using an inversion restricting the source time function to be a single triangular element of 1 s half duration (Fig. 5b). The modelled centroid depth increases (from 6 to 9 km) in an attempt to match the observed seismogram widths, though the larger event magnitude and correspondingly longer source time function produce a more pronounced change in depth here than was seen for the smaller magnitude 1994 event. This shorter, simpler source time function degrades the fit to the data, suggesting a longer rupture history but the exact details are not well constrained. We find

## 2004 February 24, Al Hoceima

298 / 83 / 179 / 6 / 3.8e18

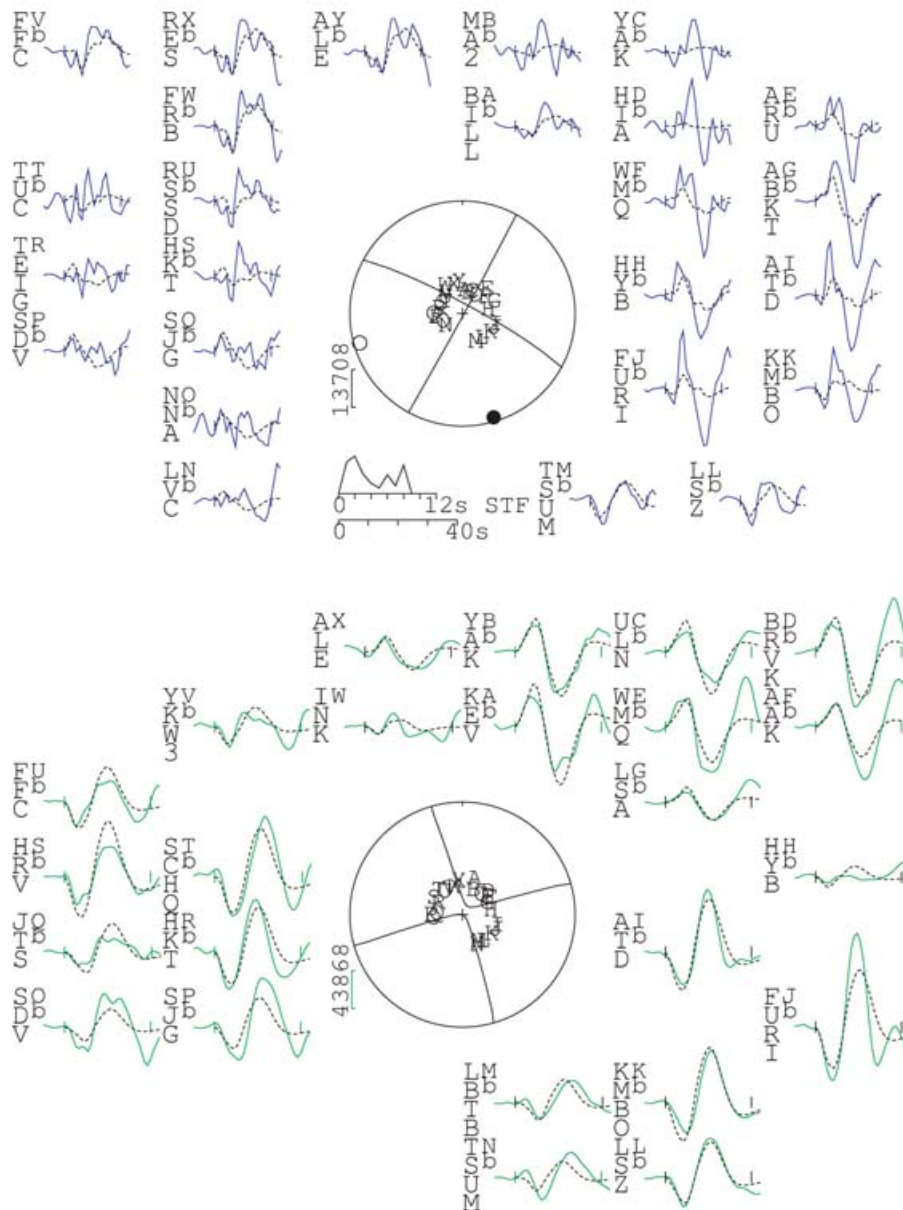


**Figure 4.** Waveform modelling results for the 2004 Al Hoceima earthquake. The minimum misfit solution shown here has strike  $298^\circ$ , dip  $83^\circ$ , rake  $179^\circ$ , depth 6 km, and scalar moment  $3.8 \times 10^{18}$  N m ( $M_w$  6.4), displayed as in Fig. 2.

a marginal, but not conclusive improvement in the fit for a rupture propagating in the direction  $118^\circ$ , with a corresponding marginal decrease for directions  $298^\circ$ ,  $028^\circ$  and  $208^\circ$ .

For source parameters from the Harvard CMT catalogue (Fig. 5c) and Stich *et al.* (2005) (Fig. 5d), the source time function producing the best fit is one that separates into many discrete pulses. At stations such as FRB(P), which plot away from the nodal planes in the focal sphere, the fit of the Harvard CMT model is comparable to that of our minimum misfit solution, but is worse for near-nodal stations. For the model of Stich *et al.* (2005), the fit at station FRB(P) is slightly better than our minimum misfit solution, but the overall fit to the SH waves is poorer.

We produce synthetic seismograms using the source geometry determined from our InSAR study and allowing the source time

function to vary in order to best fit the waveform data. The synthetic waveforms are very similar in shape to those from the minimum misfit solution, though the amplitudes, which are scaled to match the magnitude from the InSAR study, are slightly overestimated (Fig. 5e).

### 3 INSAR DETERMINATION OF SOURCE GEOMETRY

We use data from ASAR on ESA's ENVISAT satellite to create 3 interferograms spanning the 2004 earthquake, and data from ESA's archive of ERS-1 data to create two interferograms spanning the 1994 earthquake, including interferograms on both ascending and

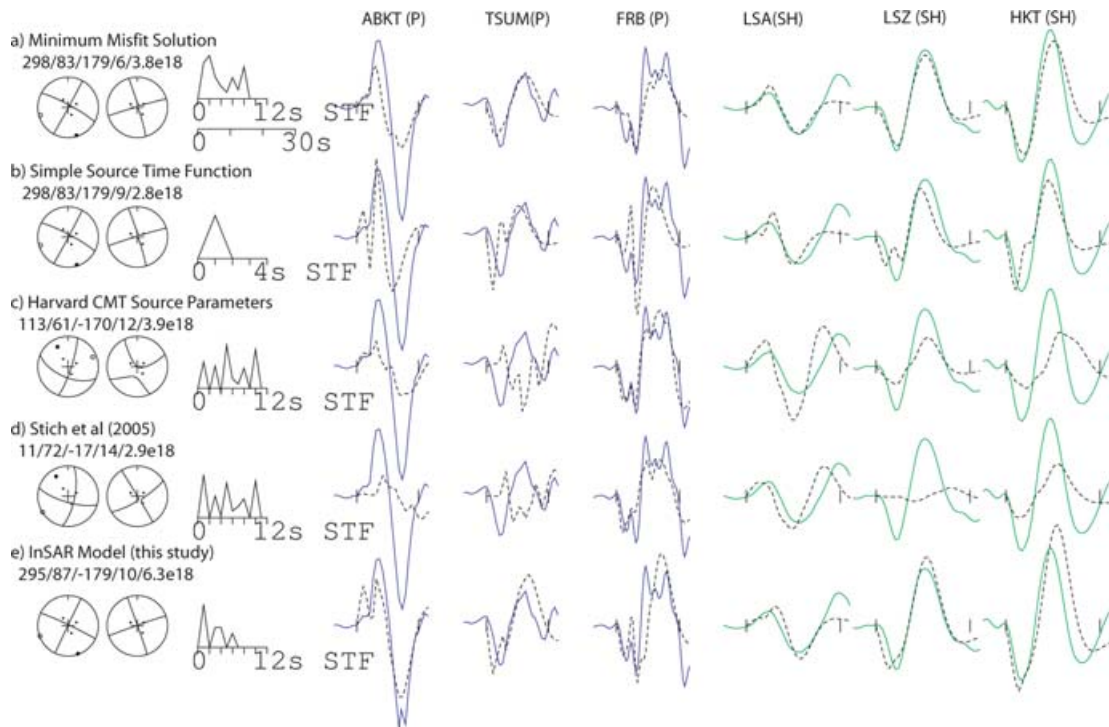


**Figure 5.** Comparison of published solutions for the 2004 Al Hoceima earthquake (Table 1), displayed as in Fig. 3. (a) The minimum misfit solution shown in Fig. 4. (b) Simple Source Time Function. As for the 1994 earthquake, the shorter source time function moved the modelled centroid to a greater depth. (c) Harvard CMT source parameters. (d) The solution of Stich *et al.* (2005). Both *c* and *d* fit well for *P* waves at stations away from the nodal planes (e.g. FRB(*P*)) but the fit to near-nodal stations and the *SH* waves is much poorer. (e) Our preferred solution determined from InSAR (model A). The synthetic waveforms are very similar in shape to the minimum misfit solution, though the larger magnitude of the InSAR model means the amplitudes are slightly over-estimated.

descending tracks for each case (Fig. 1). We process the data using JPL/Caltech ROI-PAC software (Rosen *et al.* 2004). The topographic phase is removed using a 3 arcsec  $\sim$ 90 m resolution digital elevation model (DEM) generated by the NASA Shuttle Radar Topography Mission (SRTM) (Gesch 2006), a power spectrum filter is applied (Goldstein & Werner 1998) and the interferogram is unwrapped using a branch cut method (Goldstein *et al.* 1988).

The interferograms spanning the 1994 earthquake, *ifm1*, *ifm2* (Table 2, Fig. 6), both have time spans of approximately two years. In the descending interferogram (*ifm1*), only one lobe of deformation is visible and the peak-to-trough line of sight deformation is 8 cm (3 fringes). The ascending interferogram (*ifm2*), is more coherent in the near field and shows two lobes of deformation elongated NE–SW and a peak-to-trough line of sight deformation of 10 cm (3 fringes). Qualitatively, this is consistent with a NE–SW fault

plane for the 1994 earthquake. The descending interferograms for the 2004 earthquake (*ifm3*, *ifm4*) have time spans of just over a year and baselines of 54 and 92 m respectively. These interferograms are coherent over the sparsely vegetated eastern and coastal areas but over the densely vegetated and more mountainous inland areas are incoherent. Three lobes of deformation can be seen in the data with a peak-to-trough line-of-sight displacement of  $\sim$ 22 cm (8 fringes). The ascending interferogram for the 2004 earthquake, (*ifm5*), has a shorter time span ( $\sim$ 7 months) and smaller baseline ( $\sim$ 28 m) and shows good coherence over the whole area covered. Two elongated lobes of deformation are observed with a peak-to-trough line-of-sight displacement of  $\sim$ 23 cm (8 fringes). The lobes are elongated in a NW–SE direction and the fringes pinch together in the northwest. Qualitatively, this is consistent with a NW–SE fault plane for the 2004 earthquake.

**Table 2.** Interferograms produced for the 1994 May 26 and 2004 February 24, Al Hoceima, Morocco earthquakes.

	<i>ifm1</i>	<i>ifm2</i>	<i>ifm3</i>	<i>ifm4</i>	<i>ifm5</i>
Satellite	ERS-1	ERS-1	ENV	ENV	ENV
Date 1	1993-Sep-23	1993-Nov-28	2003-Apr-13	2003-Jun-22	2003-Dec-10
Date 2	1995-Dec-30	1995-Nov-22	2004-Jun-6	2004-Jul-11	2004-Jul-7
Track	280	230	280	280	230
Pass	Desc.	Asc.	Desc.	Desc.	Asc.
$B_{\perp}$ (m)	80	40	54	92	28
$H_a$ (m)	125	250	185	109	360
Time span (days)	828	724	420	385	210

$B_{\perp}$ : Perpendicular Baseline.  
 $H_a$ : Altitude of Ambiguity.

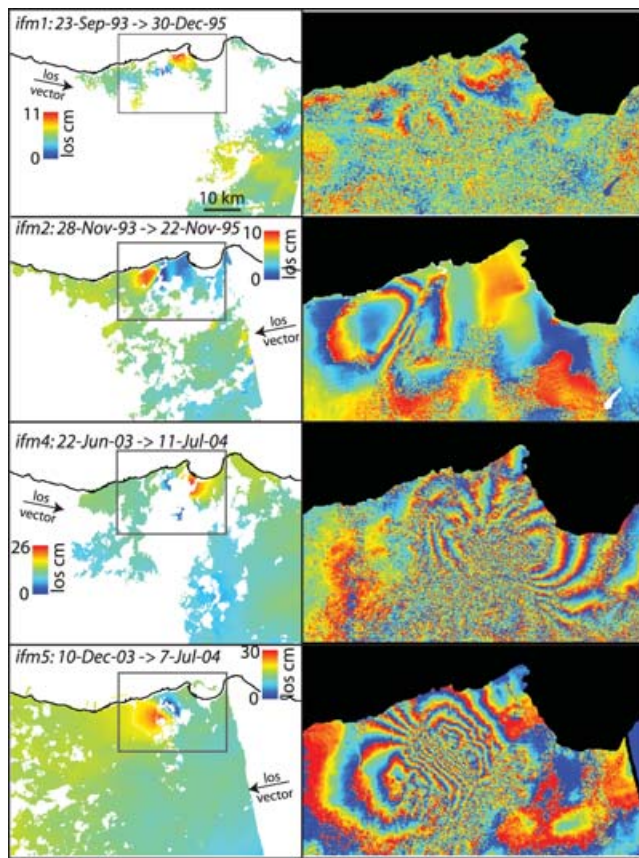


**Figure 6.** Interferograms (see Table 2). *ifm1*: Descending track coseismic interferogram for the 1994 earthquake. *ifm2*: Ascending track coseismic interferogram for the 1994 earthquake. *ifm4*: Descending track interferogram spanning the 2004 earthquake. *ifm5*: Ascending track interferograms spanning the 2004 earthquake. Right-hand column shows original interferograms before unwrapping, each fringe represents half a wavelength of deformation (2.8 cm) in the satellite line of sight. Left-hand column shows unwrapped data; unwrapping was carried out using the branch cut algorithm of Goldstein *et al.* (1988) and unwrapping errors fixed manually.

### 3.1 Uniform slip modelling for the 2004 earthquake

Ground deformation modelling based on far-field geodetic data alone is not particularly sensitive to the mechanism of the earthquake (e.g. Tsuji *et al.* 1995) so it is vital to have a high density of near-field observations. For small magnitude, buried earthquakes, this near-field area is very small and even with quite coherent interferograms, it can be difficult to identify the fault plane (e.g. Lohman *et al.* 2002; Funning *et al.* 2005).

We perform two inversions on the 2004 Al Hoceima interferograms (Table 3); model A constrains the strike to be within  $\sim 30^\circ$  of the NW–SE nodal plane determined from body wave modelling ( $90$ – $150^\circ$ ) and model B constrains the strike to be within  $\sim 30^\circ$  of the NE–SW nodal plane ( $0$ – $60^\circ$ ). We invert for uniform slip on a rectangular fault plane using the formulation of Okada (1985) for rectangular dislocations in an elastic half-space. The inversion procedure minimizes the squared misfits between the observed and the predicted satellite line of sight deformation using a non-linear, downhill simplex algorithm with Monte Carlo restarts to avoid local minima (Wright *et al.* 1999). The source parameters determined using a simple elastic half-space are very similar to those found using a more realistic layered elastic half-space, except that rigidity stratification tends to increase the magnitude of slip at depth

(Simons 2002). We use all three interferograms (*ifm3*, *ifm4*, *ifm5*) but double weight the ascending interferogram (*ifm5*) to account for the fact that the descending interferograms are almost identical. Experiments in which the bottom depth of faulting is unconstrained produce faults that extend to depths in excess of 100 km. We chose a maximum fault depth of 18 km based on the aftershock distribution from the 1994 Al Hoceima earthquake (El Alami *et al.* 1998). Errors on the parameters were estimated using a Monte Carlo simulation of correlated noise (Wright *et al.* 2003; Lohman *et al.* 2005; Parsons 2006). For each interferogram, we simulate 100 sets of correlated noise that have the same covariance function as observed in the data. The simulated noise is then added to the original interferogram to create 100 perturbed data sets. The inversion procedure is applied to each of these data sets and the distribution of best-fitting solutions provides information on the errors and trade-offs of the solution.

Both models produce a first order fit to the observed deformation pattern (Fig. 7) and fix the top of the fault at a depth of  $\sim 2$  km, consistent with the absence of a fault scarp at the surface. The rms misfit to the model based on the NE–SW nodal plane (23 mm) is marginally greater than that of the model based on the NW–SE nodal plane (21 mm). However, both are dominated by atmospheric noise and it is not possible to distinguish between the nodal planes based on misfit alone. The model based on the NW–SE nodal plane produces a pure right-lateral fault model with physically realistic fault parameters. In contrast, the model based on the NE–SW nodal plane produces a solution with a fault length of  $\sim 1.1$  km and slip of  $\sim 12.9$  m. This has a slip-to-length ratio of  $1.3 \times 10^{-2}$  which far exceeds empirical estimates of the slip-to-length ratio for intraplate earthquakes which range from  $2 \times 10^{-5}$  to  $1 \times 10^{-4}$  (e.g. Scholz 1990; Funning 2005); hence we consider this model unlikely. A third model (C) constraining the strike to within  $30^\circ$  of the NE–SW nodal plane and the slip to a more likely value of 1 m produces a more realistic slip-to-length ratio but increases the misfit to the data. Our Monte Carlo error analysis of this model finds two clusters of solutions; one with slip buried at a depth of  $\sim 1$  km and another in which the slip breaks the surface. Since no significant surface ruptures were observed we quote the solution for the first of these clusters.

Based on the rms misfits and slip-to-length ratios resulting from the inversions using uniform slip models, we conclude that for the 2004 Al Hoceima earthquake, a NW–SE primary fault plane is more consistent with the data than a NE–SW primary fault plane.

### 3.2 Uniform Slip Modelling using synthetic data

We use synthetic data to provide further insight into the behaviour of our inversion procedure in situations where models based on either nodal plane produce similar deformation patterns. This approach has the advantage that, unlike real data, we know in advance which nodal plane is the fault plane.

The synthetic example used here is a buried, vertical, right-lateral, strike-slip fault with a strike of  $120^\circ$  and fault geometry given in Table 4. Using the formulation of Okada (1985) for rectangular dislocations in an elastic half-space, we produce synthetic interferograms for both ascending and descending tracks. Initially we use perfect data without any noise or decorrelation effects (i.e. complete coverage) but reduce the number of data points for inversion by resampling using a quadtree algorithm (e.g. Jonsson *et al.* 2002).

We perform two inversions: Model 1 constrains the strike to lie in the range  $90$ – $150^\circ$ ; and model 2 constrains the strike to lie in the range  $0$ – $60^\circ$ . Models based on either of the nodal planes are

**Table 3.** Source parameters of the 1994 May 26 and 2004 February 24, Al Hoceima, Morocco earthquakes based on various source models. 1994A: NE–SW nodal plane; 1994B: NW–SE nodal plane. 2004A: NW–SE nodal plane. 2004B: NE–SW nodal plane. 2004C: NE–SW nodal plane with fixed slip of 1 m. 2004D: Distributed slip on a NW–SE nodal plane.

Model	2004A (preferred)	2004B	2004C	2004D	1994A (preferred)	1994B
Orientation	NW–SE	NE–SW	NE–SW	NW–SE	NE–SW	NW–SE
Strike (°)	295.4 ± 1.1	203.0 ± 1.1	203.7 ± 2.0	295 <sup>a</sup>	23.3 ± 4.5	113.2 ± 8.1
Dip (°)	87.4 ± 1.5	88.3 ± 2.3	83.8 ± 4.7	88 <sup>a</sup>	86.9 ± 2.3	74.4 ± 7.2
Rake (°)	−179.2 ± 1.2	−1.2 ± 1.6	−8.4 ± 3.7	−179 <sup>a</sup>	−1.2 ± 2.6	−178.6 ± 2.8
Slip (m)	1.4 ± 0.1	12.9 ± 2.1	1 <sup>a</sup>	0.50 <sup>b</sup>	0.69 ± 0.06	0.90 ± 0.56
Length(km)	8.8 ± 0.4	1.1 ± 0.3	8.2 ± 1.0	17 <sup>b</sup>	9.9 ± 1.4	4.7 ± 1.6
Min. Depth (km)	2.1 ± 0.2	3.6 ± 0.2	0.9 ± 0.5	2 <sup>b</sup>	2 <sup>a</sup>	2 <sup>a</sup>
Max. Depth (km)	18 <sup>a</sup>	18 <sup>a</sup>	18 <sup>a</sup>	18 <sup>b</sup>	12 <sup>a</sup>	12 <sup>a</sup>
Slip/Length (× 10 <sup>−5</sup> )	16	1300	12	13 <sup>b</sup>	6.9	19
rms misfit (mm)	21	23	26	19	9	10
Lat	−3.986 <sup>c</sup>	−3.979 <sup>c</sup>	−3.982 <sup>c</sup>	−4.002 <sup>d</sup>	−4.058 <sup>c</sup>	−4.061 <sup>c</sup>
Long	35.137 <sup>c</sup>	35.135 <sup>c</sup>	35.138 <sup>c</sup>	35.139 <sup>d</sup>	35.201 <sup>c</sup>	35.197 <sup>c</sup>
Moment (× 10 <sup>18</sup> Nm)	6.2	5.9	4.7	7.4	2.1	1.2
Magnitude ( <i>M<sub>w</sub></i> )	6.5	6.4	6.4	6.5	6.2	6.0

<sup>a</sup> Parameters fixed during inversion.

<sup>b</sup> For the distributed slip model (D), we follow the definitions of Funning (2005) and define the dimensions of the fault by finding the slip contour within which 95 per cent of slip occurs. The mean slip is the average slip within this contour.

<sup>c</sup> For uniform slip models, the location is defined as the centre of the uniform slip plane projected vertically to the surface.

<sup>d</sup> For distributed slip models, the centroid is given as the location.

capable of producing a reasonable fit to the first-order deformation pattern. By accurately reproducing all parameters, the model based on the fault plane (NW–SE) confirms that, due to the spatial correlation of the signal, little or no relevant information is lost using the quadtree resampling (Table 1). In contrast, the model constrained to the auxiliary plane (NE–SW) requires a short fault (2 km) with high slip (9.1 m). This gives a slip-to-length ratio of  $5 \times 10^{-3}$  which far exceeds empirical estimates of the slip-to-length ratio for intraplate earthquakes (e.g. Scholz 1990; Funning 2005). For these models, the root mean square (rms) misfit to the NW–SE model is significantly lower than to the NE–SW model.

We repeat the experiment including the effects of decorrelation and atmospheric noise (Models 3 and 4). The synthetic data are perturbed randomly using noise based on 1-D covariance function derived from the real Al Hoceima interferograms (Hanssen 2001; Wright *et al.* 2006; Lohman *et al.* 2005) and a coherence mask based on the real interferograms is applied. In this case, the same phenomenon is observed, but the rms misfits are dominated by atmospheric noise, so that, while the misfit to the model based on the fault plane is still lower, the difference between the two values is much less.

In order to extend this result from the specific geometry of a NW–SE fault to the more general case of a buried strike-slip earthquake, we repeat the experiment using synthetic data created assuming a NE–SW fault plane. Again, the inversion which assumed the auxiliary plane to be the fault plane produces a fault model with an extremely high slip-to-length ratio, while the inversion which assumes the correct nodal plane to be the fault plane identifies the synthetic fault parameters well. This result is a property of geodetic data for buried strike-slip earthquakes and is independent of factors such as fault geometry, missing data caused by decorrelation, and atmospheric noise.

For a point source, the pattern of ground deformation is identical whichever of the nodal planes is used as the fault plane. As the fault length increases, the deformation pattern becomes increasingly elongated and for long faults (>20 km), the fault plane is clearly defined, even by visual inspection alone. For short faults, the asym-

metry is less and can be partly obscured by atmospheric noise and patches of incoherence. Nevertheless, the inversion procedure is capable of identifying these small differences and correctly identifying the fault plane.

The results of our synthetic experiment support our conclusions that the NW–SE nodal plane was the fault plane in the 2004 earthquake. Synthetic models assuming the auxiliary plane to be the fault plane produce an unrealistic slip-to-length ratio as does the model assuming the NE–SW nodal plane was the fault plane in the 2004 earthquake.

### 3.3 Distributed slip modelling for the 2004 earthquake

Once the correct orientation of the fault plane has been identified, the model can be refined by solving for the distribution of slip on the fault. Using the fault geometry for a NW–SE fault plane determined using uniform slip modelling and extending it along strike and downdip, we subdivide the fault into an array of 24 by 18 square elements each measuring 1 km by 1 km. Following the method of previous authors (e.g. Du *et al.* 1992; Jonsson *et al.* 2002; Wright *et al.* 2003), the following equation (1) can then be solved to find the slip on each element,  $\mathbf{m}$  using a non-negative least-squares algorithm (Bro & De Jong 1997)

$$\begin{pmatrix} \mathbf{A} \\ \gamma^2 \nabla^2 \end{pmatrix} (\mathbf{m}) = \begin{pmatrix} \mathbf{d} \\ 0 \end{pmatrix} \quad (1)$$

where  $\mathbf{A}$  is the matrix of Green's functions containing the line-of-sight displacement resulting from 1m of slip on each element calculated using the elastic dislocation formulation of Okada (1985);  $\nabla^2$  is the finite difference approximation of the Laplacian smoothing operator used to prevent unphysical short wavelength slip variations and  $\gamma^2$  is the scalar weight factor which determines the weighting of the smoothing. For high values of  $\gamma^2$ , the solution is over-smooth and fits the data poorly; for low values the fit to the data is good, but the solution contains unphysical variations in slip. A good value is chosen by plotting solution roughness, defined to be the mean absolute

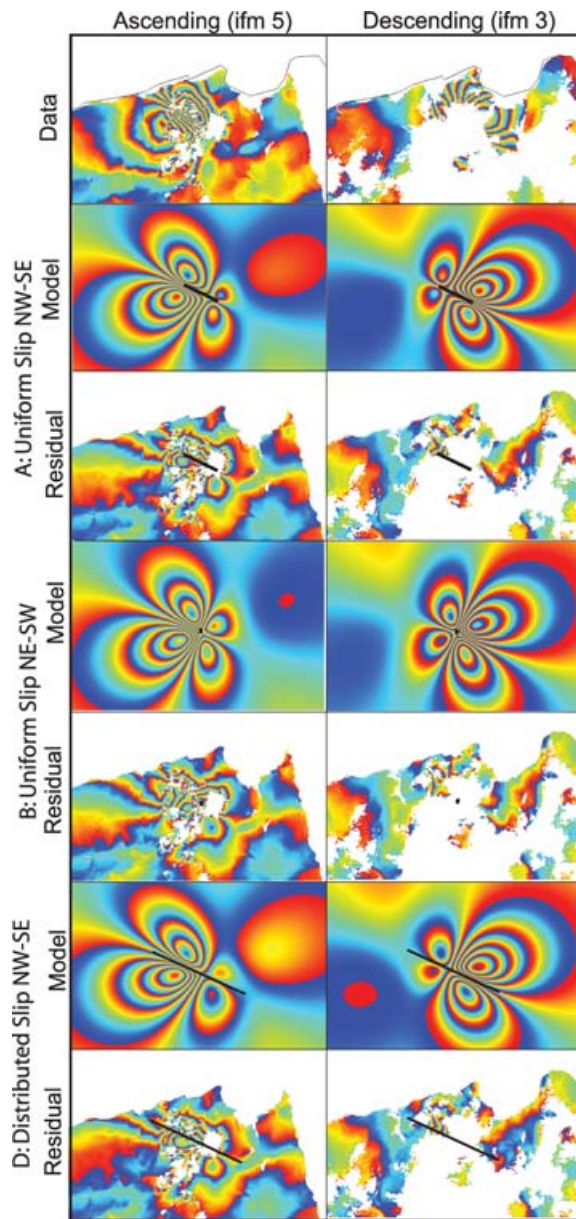


**Figure 7.** Models and residuals for uniform slip inversions for 2004 earthquake. A.:NW–SE nodal plane. B: NE–SW nodal plane. D: Distributed slip on a NW–SE nodal plane. Each fringe represents 2.8 cm of line-of-sight displacement.

Laplacian, against misfit for a range of  $\gamma$  (Fig. 8e). This compares well with the optimum value found using Akaike's Bayesian Information Criterion (ABIC) (Yabuki & Matsu'ura 1992; Fukahata *et al.* 2004; Funning 2005).

The resulting slip distribution is elliptical in shape with a maximum slip of 2.1 m in the centre of the fault at a depth of  $\sim 8$  km and  $\leq 14$  cm in the top 1 km, consistent with observations (Fig. 8a). Model interferograms and residuals based on this slip distribution are shown in Fig. 7. The rms misfit to the data is reduced to 19 mm.

As for our uniform slip models, we investigate the errors on the solution by applying the inversion to 100 perturbed data sets with the same noise characteristics as the interferograms. The standard

**Table 4.** Source parameters for a synthetic buried strike-slip earthquake based on various source models. Synthetic: Parameters for synthetic buried strike-slip earthquake. 1,3: NW–SE nodal plane. 2,4: NE–SW nodal plane.

Model	Synthetic	1	2	3	4
Orientation	NW–SE	NW–SE	NE–SW	NW–SE	NE–SW
Noise	–	No	No	Yes	Yes
Coherence Mask	–	No	No	Yes	Yes
Strike ( $^{\circ}$ )	300	300	30	301	32
Dip ( $^{\circ}$ )	90	90	90	88	89
Rake ( $^{\circ}$ )	–180	–180	1	179	2
Slip (m)	1.0	1.0	9.1	1.0	8.4
Length(km)	10.0	10.0	2.0	11.0	2.0
Min. Depth (km)	2	2	5	2	5
Max. Depth (km)	18	18	12	15	12
Slip/Length ( $\times 10^{-5}$ )	10	10	500	9	400
rms (mm)	–	0.2	6	9	11

deviation of the solutions gives a measure of the error on the amount of slip on each element (Fig. 8b). The errors increase with depth reaching a maximum of  $\sim 12$  cm at a depth of  $\sim 12$  km.

The resolution matrix,  $\mathbf{R}$  is given by the solution to,

$$[\mathbf{A}_s^T \mathbf{A}_s] \mathbf{R} = \mathbf{A}^T \mathbf{A} \quad (2)$$

where  $\mathbf{A}_s$  is the matrix,  $[\mathbf{A} \gamma^2 \nabla^2]^T$  of Green's functions with smoothing. We invert for each column of  $\mathbf{R}$  using a non-negative least-squares inversion. Each column contains the model parameters found when inverting synthetic data produced by placing 1 m of slip on the corresponding element (Menke 1989; Du *et al.* 1992). If the model is perfectly resolved,  $\mathbf{R}$  will be an identity matrix. We define the horizontal and vertical resolution lengthscale at each element to be the total dimensions of the elements in the horizontal and vertical direction for which the value in the resolution matrix is greater than  $1/e$  of the maximum (Figs 8c and d). At the depth of peak slip the horizontal resolution is 13 km and the vertical resolution 11 km, comparable to the dimensions of the fault. For earthquakes of this size, and smaller, modelling slip distributed over a fault plane appears not to be a significant improvement over the simpler, uniform slip model. Indeed the rms misfit to the distributed slip inversion (19 mm) is not significantly lower than for the uniform slip inversion (21 mm). The resolution of the model could be improved by reducing the weighting of the smoothing parameters, but while this would reduce the misfit to the data (Fig. 8e), the errors on the slip distribution would increase (Backus & Gilbert 1970; Wright *et al.* 2006).

### 3.4 InSAR model of 1994 earthquake

The focal mechanism of the 1994 Al Hoceima earthquake is very similar to that of the 2004 event but previous studies (e.g. Bezzeghoud & Buforn 1999; Calvert *et al.* 1997) favour a NE–SW trending fault plane. The interferograms constructed for the 1994 earthquake are less coherent than for the 2004 earthquake and the observed pattern of deformation is incomplete. Nevertheless, we use the same uniform slip inversion and error estimation procedures as described previously and produce two models, one assuming that each of the nodal planes is the fault plane (Fig. 9). As expected, the Monte Carlo error analysis shows the solutions are less well constrained than for the 2004 earthquake and we see significant trade-offs between strike and position, slip and length, moment and length. The solutions are primarily determined by the ascending interferogram, which is more coherent in the near field.

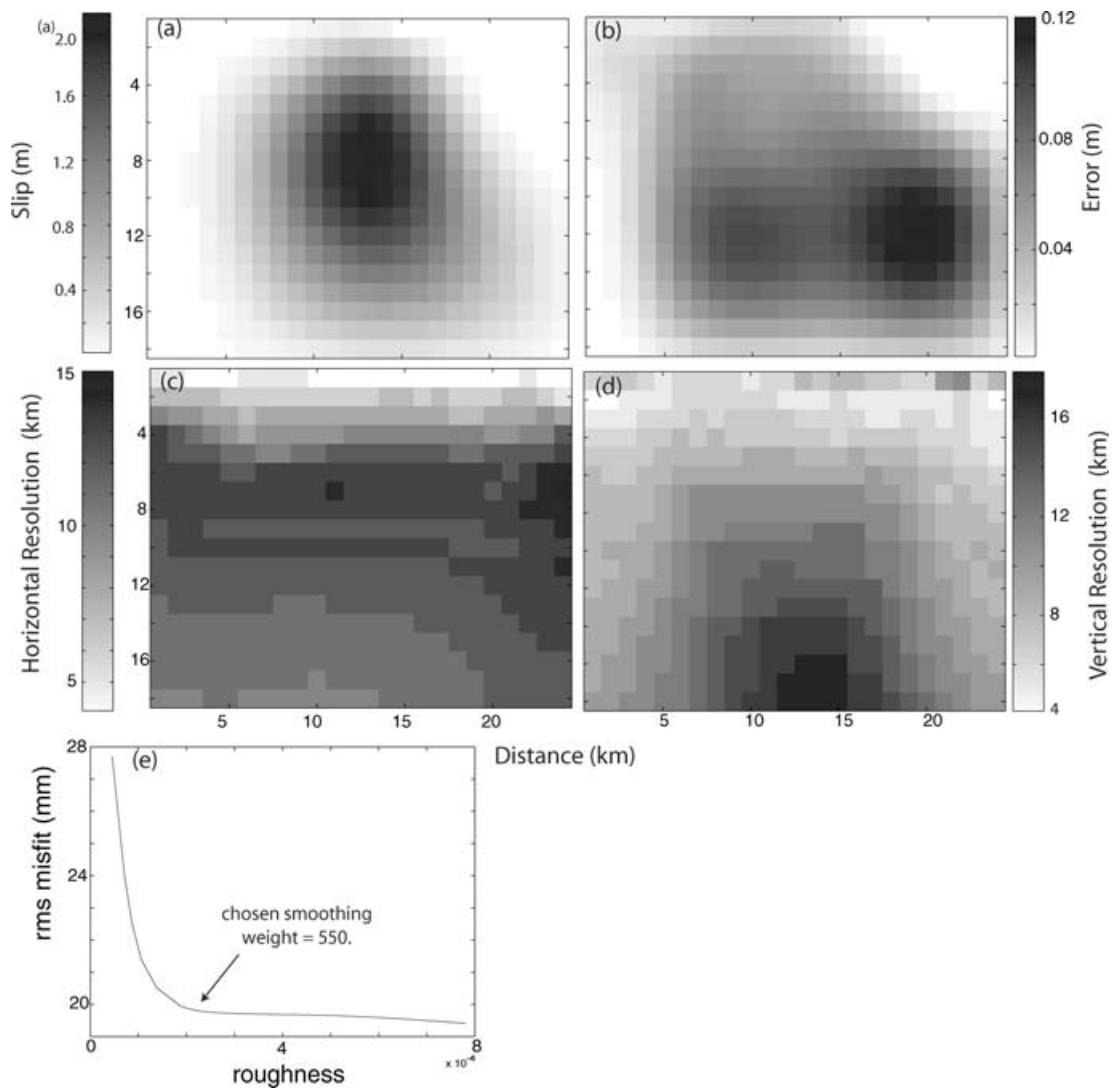


**Figure 8.** Model, Errors and Resolution of the distributed slip inversion for the 2004 Al Hoceima, Morocco earthquake. Vertical axis represents depth (km). (a) Slip on the fault plane. (b) Errors on the slip calculated using a Monte Carlo Error estimation technique. (c) Horizontal resolution lengthscales. We define the resolution at each element to be the number of elements in the horizontal and vertical direction for which the value in the resolution matrix is greater than  $1/e$  of the maximum. (d) Vertical resolution lengthscales. (e) Trade-off curve for misfit and roughness for distributed slip solution. This is used to find a good weight factor for the smoothing.

As with the 2004 earthquake, both models fit the first order pattern of deformation and the rms misfits are not significantly different. The slip-to-length ratio is larger for the NW–SE model (1994B) than the NE–SW model (1994A) but both lie within the range of parameters considered to be ‘physically reasonable’. In this case, the InSAR data appears to be incapable of distinguishing which of the nodal planes is the fault plane.

We have been able to distinguish between the primary fault plane and auxiliary plane using InSAR observations in the case of the 2004 earthquake, but not for the 1994 earthquake. In part, this is because the 1994 earthquake is closer to the coast and a significant proportion of the deformation pattern is offshore. However, in general, the nodal plane ambiguity will also be harder to resolve for smaller magnitude earthquakes. The amount of ground deformation for the 1994 earthquake (3 fringes) is smaller than for the 2004 earthquake (8 fringes), but the level of atmospheric noise remains unchanged. The lower signal-to-noise ratio means all the source parameters are

less well resolved reducing our ability to distinguish between nodal planes. The smaller magnitude might also be expected to correspond to a shorter fault length. As shown by our synthetic experiments, the closer the source becomes to a point, the more difficult it is to distinguish between nodal planes based on the deformation pattern. In this case, comparing the fault lengths from the best-fitting models of the 1994 and 2004 earthquake shows no statistically significant difference in fault length. However, the source parameters for the 1994 earthquake are less well resolved and there are significant trade-offs between fault length, slip and fault depth.

Regardless of which nodal plane is considered to be the fault plane, the InSAR data is capable of improving the accuracy of the earthquake location over previous seismological estimates. Both models locate the 1994 earthquake  $\sim 11$  km to the NW of the 2004 earthquake (Fig. 9). We conclude that the spatial distribution of our data is not sufficient to determine the orientation of the fault, but does provide useful constraints on location.

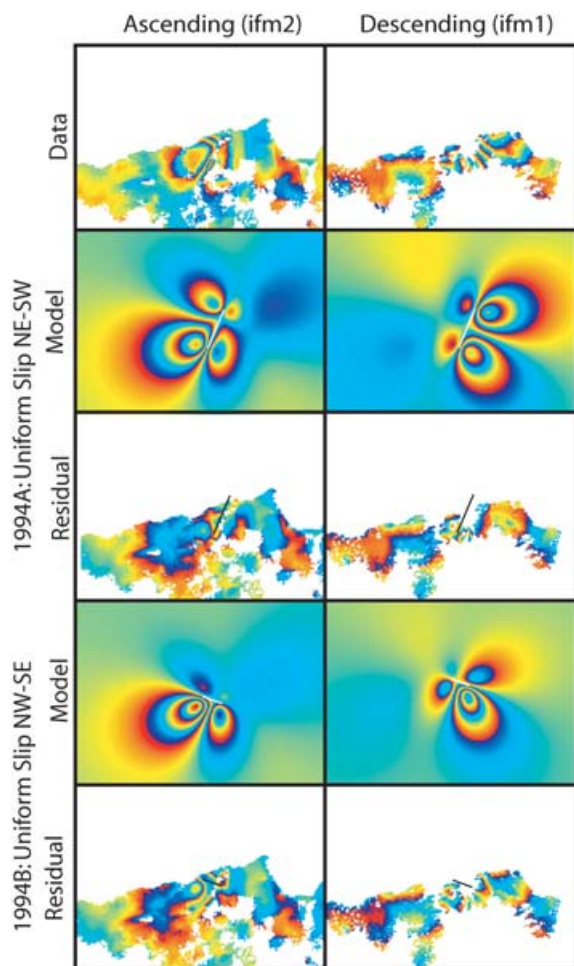


**Figure 9.** Models and residuals for uniform slip inversions for the 1994 earthquake. A: NE–SW fault plane. B: NW–SE fault plane.

## 4 MULTIPLE EVENT RELOCATION OF THE AL HOCEIMA EARTHQUAKE SEQUENCE

### 4.1 Relative locations

The epicentral pattern of the 1994 and 2004 earthquake sequences is investigated by a multiple event relocation study using the hypocentroidal decomposition method (HDC) of Jordan & Sverdrup (1981). By relocating a cluster of earthquakes from a limited source region simultaneously, path-correlated traveltime errors can be removed from the problem and the relative locations of the events can be determined with greater accuracy. The HDC method is distinguished by the separation of the problem into two quite separate problems, estimation of the relative locations of events in the cluster (cluster vectors), followed by location of the entire cluster as if it were a single earthquake, whose location is defined by the hypocentroid. This two-step process is repeated iteratively several times to convergence. An important part of the analysis is the progressive identification and flagging of outlier readings based on analysis of the path-corrected ‘cluster residuals’ of all arrival time readings for a given station-phase combination. This is done between successive runs of the program.

A cluster of earthquakes in the Al Hoceima region is assembled by searching the catalogues of the ISC and the USGS’s Preliminary

Determination of Epicenters (PDE) catalogue for earthquakes in the period 1964–2004, in a radius of approximately 75 km from the 2004 epicentre. A preliminary cluster of 90 events was trimmed to 58 events within about 40 km of the 1994 and 2004 main shocks through a series of preliminary relocations that identified earthquakes with poor data quality based on inspection of the confidence ellipses. For the earthquakes selected, between 17 and 446 station-phase combinations were available for each, with station azimuths ranging from 30° to 230°. The largest semi-axis of a cluster vector 90 per cent confidence ellipse is 7.3 km. In the final cluster of 58 earthquakes, ten are associated with the 1994 event and its aftershocks through 1994 October; 19 are associated with the 2004 event and its aftershocks through 2004 June.

Prior to the HDC analysis, cluster events are relocated individually to determine the best source depth. Depth is fixed in the HDC analysis because only a few events have adequate arrival time data (i.e. depth phases) to estimate depth as a free parameter. A default depth of 10 km is used when there is insufficient data to constrain the depth. Errors in assumed depth of 10–20 km have little influence on the epicentres estimated in the HDC analysis. The hypocentres of the 1994 and 2004 main shocks are set at 10.1 and 9.2 km, respectively, based on the waveform modelling and inferred slip distributions described elsewhere in this study.

The HDC analysis uses arrival time data for all primary and most secondary body wave phases at all epicentral distances greater than 3.0 degrees. Traveltimes and derivatives are calculated from the ak135 model (Kennett *et al.* 1995), corrected for ellipticity and station elevation. Phase identification for all readings is done in a probabilistic manner, similar to the method described by Engdahl *et al.* (1998) for re-identifying depth phases. Readings are weighted according to station-phase specific estimates of reading error, based on analysis of the path-corrected cluster residuals in preliminary HDC inversions. Additional weighting is done on a phase-specific basis to account for observed departures of different phases from the ak135 traveltime model (e.g. Kennett *et al.* 1995).

HDC analysis results in changes of as much as 40 km in the relative locations of these earthquakes, using ISC and PDE locations as starting locations. For 24 events the change in relative location exceeded 10 km. For most events the relative location is determined to within a few km at the 90 per cent confidence level.

The aftershocks of the 1994 and 2004 earthquakes define a zone which could be interpreted as either a single curved fault or a pair of faults perpendicular to each other (Fig. 10a). While many strike-slip faults are curved (e.g. Denali Fault, Alaska), the change in strike occurs over a much greater distance and the resulting space problems are accommodated by secondary faulting. If we explain the Al Hoceima aftershock patterns with a single curved strike-slip fault, the strike of the fault would have to change by 90° over a distance of only ~30 km. We prefer to interpret the pattern as a pair of conjugate strike-slip faults corresponding to the nodal planes from our bodywave seismology and InSAR studies.

Both the 1994 and 2004 earthquakes have aftershocks that occur on both faults. While previous studies have indicated that large earthquakes can rupture two conjugate faults (Robinson *et al.* 2001), we prefer, for simplicity, to assume that each earthquake occurred on a single fault and the resulting stresses triggered aftershocks on the conjugate fault (Das & Scholz 1981; Stein 1999).

### 4.2 Absolute locations

Because of unmodelled lateral heterogeneity in the Earth, the absolute (geographic) location of the cluster, determined by minimizing

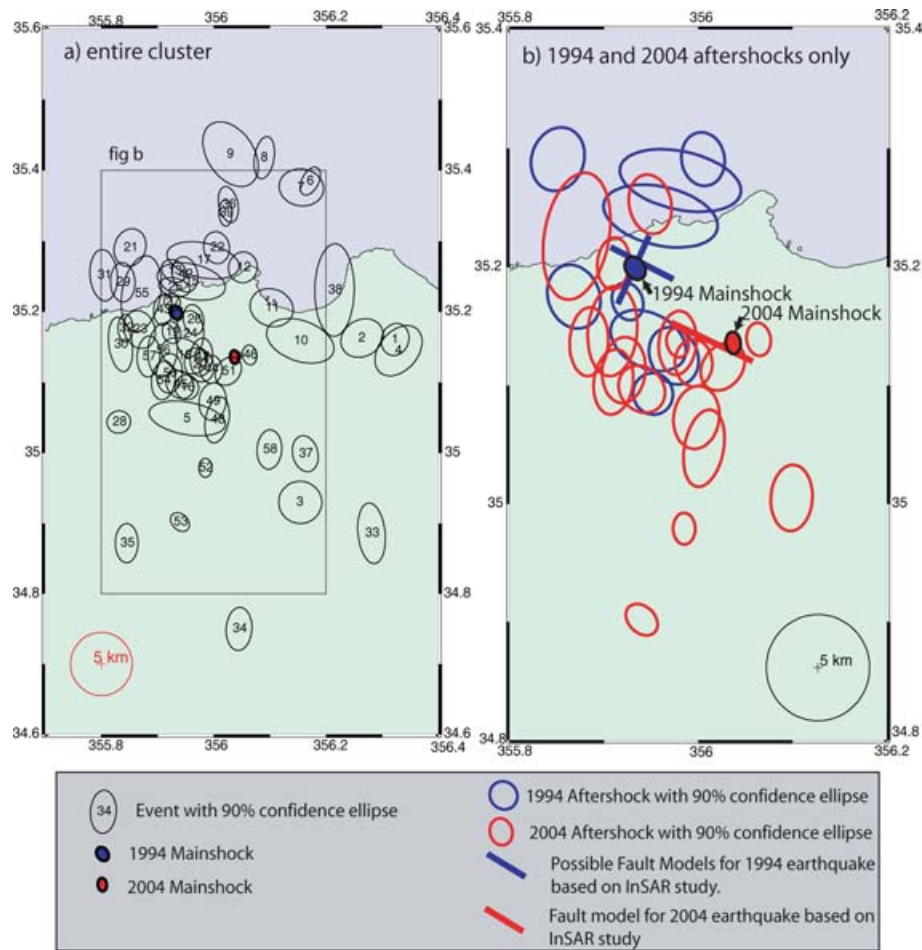


**Figure 10.** Multiple Event Relocation for the Al Hoceima Region. (a) Cluster of 58 events from 1964 to 2004. Error ellipses are shown at the 90 per cent confidence level. (b) Aftershock sequences from the 1994 (blue) and 2004 (red) earthquakes. The locations of the 2004 aftershocks match well with the NW–SE model determined using InSAR. The locations of the 1994 aftershocks show no relation to the NW–SE fault model determined using InSAR suggesting the 1994 earthquake occurred on a NE–SW fault.

the traveltimes residuals relative to the ak135 model, is expected to be biased. Studies with ground truth data suggest this bias can be as much as 15 km for a cluster, and even larger for individual earthquakes. For this study, we use HDC only to determine more accurate relative locations of the cluster events, and calibrate the absolute location of the cluster by referencing the main shocks to the fault planes determined by analysis of InSAR data. The relative location of the 1994 and 2004 main shocks is very strongly constrained by the seismic data, because so many stations observed both events. The vector between the two events is maintained in our choice of reference locations for them along their respective fault planes. Because the 1994 and 2004 fault planes are conjugate to one another, a strong constraint is placed on the absolute location of the cluster's hypocentroid, and therefore, on the epicentres of all the individual earthquakes. It is worth noting that differences in the signal-to-noise ratio for events of significantly different magnitude (i.e. main shocks and aftershocks) may lead to systematic discrepancies in picking. The relative location of the main shocks with respect to the aftershocks may thus be biased and the associated uncertainties underestimated.

The most reasonable match to the observed data (both seismological and InSAR) places the epicentre of the 1994 main shock near the centre of the inferred NE–SW trending fault plane, and places the epicentre of the 2004 main shock about 2/3 of the distance toward

the eastern end of the inferred NW–SE fault plane. The absolute locations of the aftershocks of the 1994 and 2004 are compared with the InSAR models of the earthquakes in Fig. 10(b). The 90 per cent confidence ellipses plotted in Fig. 10(b) include both the uncertainty in relative locations based on the HDC analysis, and the uncertainty in the 'ground truth' locations of the 1994 and 2004 main shocks that were used to calibrate the absolute location of the cluster. The ground truth locations are both assigned a 90 per cent confidence ellipse with semi-minor axis length 1.0 km, semi-major axis length 2.0 km, and with the semi-major axis oriented along strike.

The majority of the aftershocks of the 2004 earthquake lie along, or slightly to the south of the 2004 InSAR fault model with a few along the conjugate NE–SW fault. Although aftershocks from the 1994 earthquake occur along both the NW–SE and NE–SW faults, the NW–SE fault defined by the aftershocks is not aligned with the NW–SE InSAR fault model. We conclude that it is most likely that the 1994 earthquake occurred on the NE–SW fault and the 2004 earthquake occurred on the NW–SE fault.

## 5 DISCUSSION

The Eurasia–Nubia plate velocity in the Western Mediterranean is small ( $\sim 5 \text{ mm yr}^{-1}$ ) and earthquake magnitudes rarely exceed 5 (on the 420 km of plate boundary shown in Fig. 12, only

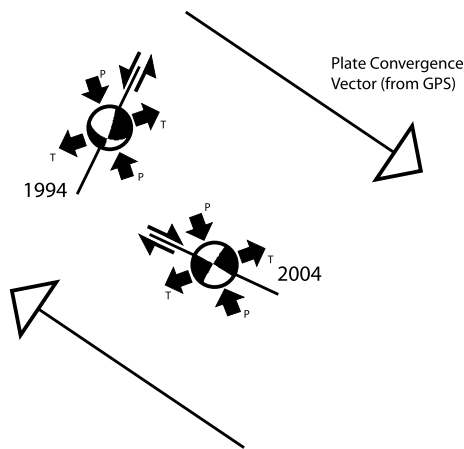


**Figure 11.** Schematic conjugate fault model for the Al Hoceima Shear Zone.  $P$  and  $T$  axes of the two earthquakes are shown and are consistent with the plate motion vector determined from GPS (McClusky *et al.* 2003)

28  $M = 5-6$  earthquakes have occurred in the last 25 yr, and only four  $M > 6$ ). While small earthquakes and microseismicity can help identify active structures and the overall stress regime, large earthquakes accommodate the majority of the strain across the plate boundary and are key to understanding kinematics. The 1994 and 2004 Al Hoceima earthquakes are the largest to occur in Morocco in the last century and so are vital to our understanding of the tectonics of the region.

The combination of results in this study suggests that the 1994 Al Hoceima Earthquake occurred on a left-lateral fault striking  $\sim 26^\circ$  and the 2004 Al Hoceima Earthquake occurred on a right-lateral fault striking  $\sim 295^\circ$ . Previous tectonic models of the region have proposed a bookshelf model of block rotation with NNE–SSW left-lateral faults (Dillon *et al.* 1980; Meghraoui *et al.* 1996; Calvert *et al.* 1997). Our observations of the 2004 earthquake suggests minor modification to such models. We consider the region to be a zone of distributed shear with strain taken up on a pair of conjugate faults (Fig. 11). The  $P$  and  $T$  axes of the 1994 and 2004 earthquakes are almost identical, despite the fault planes being perpendicular, and are consistent with this model.

A remarkable similarity exists between the Al Hoceima earthquakes and the 1987 Superstition Hills, California earthquake se-

quence. An  $M_s$  6.2 event ruptured the NE–SW left-lateral Elmore Ranch Fault, a cross fault perpendicular to the NW–SE zone of distributed shear. Eleven hours later, a  $M_s$  6.6 event occurred on the NE–SW right-lateral Superstition Hills main fault (Hudnut *et al.* 1989). The first event is thought to have reduced the normal stress on the main fault. The geometry of the two earthquake sequences is very similar and it is reasonable to assume the stress transfer would also have been similar. The time difference between the two Al Hoceima earthquakes (11 yr) is much greater than for the Superstition Hills sequence (11 hr), either suggesting a different initiation mechanism is responsible, or reflecting the different times of the two faults in their seismic cycles.

In the example of the Superstition Hills earthquake sequence and other examples of conjugate strike-slip faulting, such as the Bingol/East Anatolian Fault, Turkey (Milkereit *et al.* 2004) and the Dasht-e-Bayaz/Abiz Faults, Eastern Iran, (Berberian *et al.* 1999; Walker *et al.* 2004), one fault is clearly identifiable as the main fault, with a secondary cross fault. The situation with two roughly equal size faults is not stable, and we would expect one fault, in this case probably the NW–SE fault, to evolve into a more major structure.

Even retrospectively, with well-defined location and orientation, it has not been possible to identify either fault using remote sensing data such as Landsat imagery and Digital Elevation Models. This area is not ideal for geomorphological studies since the topography and drainage are dominated by previous structures and the faults do not reach the surface. Nonetheless, we would expect a strike-slip fault which had undergone several earthquakes to create some observable surface features. The absence of any such features leads us to suspect that the Al Hoceima earthquakes occurred on faults which may have formed recently.

Further east along the plate boundary, there is a well-defined zone of thrust faulting in Algeria,  $\sim 200$  km to the east of Al Hoceima with two recent large earthquakes, 1980  $M_s$  7.3 El Asnam and 2003  $M_w$  6.8 Zemmouri. In both cases, the earthquakes occurred on faults dipping  $50-60^\circ$  SE and striking NE, and have slip vectors approximately parallel to the plate velocity (e.g. Yielding *et al.* 1981; Meghraoui *et al.* 2004). In this region, smaller earthquakes often show strike-slip mechanisms similar to that of the Al Hoceima earthquakes (Fig. 12).

The slip vector of the 2004 Al Hoceima earthquake (Fig. 12) is parallel to the Nubia–Eurasia plate velocity as measured using

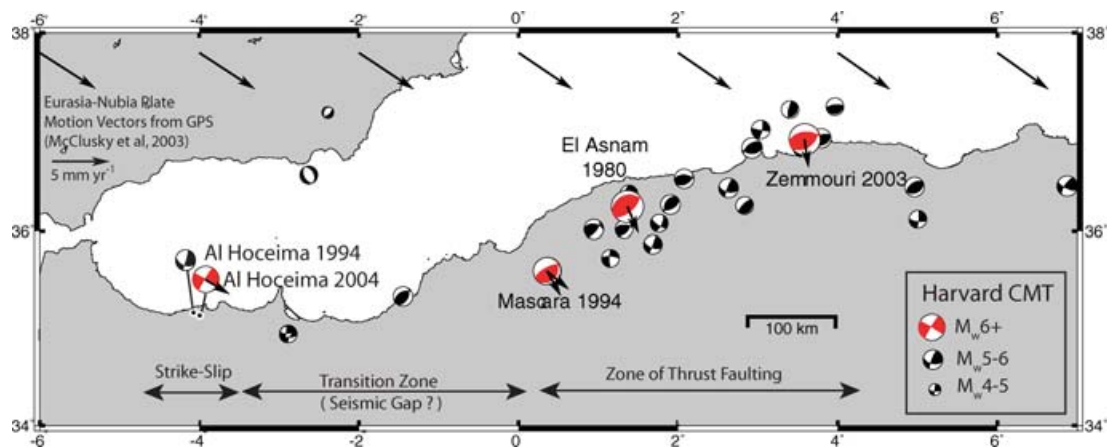


**Figure 12.** The north coast of Morocco and Algeria showing recent large earthquakes. The nature of the plate boundary between the strike-slip faulting in Al Hoceima, Morocco and the thrust faulting in Algeria is unknown. Arrows give the Eurasia–Nubia plate velocity (McClusky *et al.* 2003). Slip vectors are shown for earthquakes of magnitude 6+ (two possible slip vectors are shown for the Mascara earthquake).

GPS (McClusky *et al.* 2003). The mechanisms by which the plate motion is accommodated depends on the local orientation of the plate boundary zone. Areas in which the plate boundary is parallel to the plate motion, such as Al Hoceima, will be dominated by strike-slip faulting. In areas where the plate boundary is perpendicular to the plate motion, there will be pure thrusting; and in areas where the plate boundary is oblique to the plate motion, such as northern Algeria, there will be a mixture of thrust and strike-slip faulting. The region between Al Hoceima and Mascara has few recorded earthquakes (Fig. 12), although it must be actively deforming and further study is warranted.

## 6 CONCLUSIONS

Initial seismological and field-based observations of the 2004 Al Hoceima earthquake were ambiguous, suggesting the earthquake could have occurred on either a left-lateral NE–SW fault plane or a right-lateral NW–SE fault plane. From synthetic modelling of a buried strike-slip fault we have demonstrated that models based on either nodal plane are capable of reproducing the first order pattern of ground deformation. However, an inversion of synthetic data based on the assumption that the auxiliary plane is the fault plane will produce an unrealistically high slip-to-length ratio. Deformation patterns seen in coseismic interferograms for the 2004 Al Hoceima earthquake can, to the first order, be fitted with either a NW–SE right-lateral fault or a NE–SW left-lateral fault. The NE–SW fault model produces an unrealistically high slip-to-length ratio on a short fault, suggesting that the NE–SW nodal plane is the auxiliary plane. We conclude that the fault plane of the 2004 Al Hoceima, Morocco earthquake is orientated NW–SE.

We investigated the epicentral pattern of the 1994 and 2004 earthquake sequences by a multiple event relocation study using the hypocentroidal decomposition method, with the locations of the 1994 and 2004 earthquakes from the InSAR study as reference locations. The aftershock locations of the 1994 earthquake are consistent with a fault plane orientated NE–SW. We conclude that the two earthquakes occurred on a pair of conjugate faults in a right-lateral zone of distributed shear orientated NW–SE.

The nature and location of faulting along the ~200 km of plate boundary between the strike-slip faulting of the Al Hoceima region and the thrust faulting near the El Asnam and Zemmouri earthquakes is unclear. This area warrants a careful geomorphological study to assess the seismic hazard posed by structures which are potentially active and may be accommodating significant amounts of Nubia–Eurasia plate motion.

## ACKNOWLEDGMENTS

This work was supported by the Natural Environmental Research Council (NERC) through the Centre for the Observation and Modelling of Earthquakes and Tectonics (COMET) as well as through studentships to JB and BE. We thank Rowena Lohman and Denis Hatzfeld for helpful reviews. All ERS SAR and ENVISAT ASAR data are copyrighted by the European Space Agency and were provided under project AOE-621.

## REFERENCES

Ait Brahim, L., Chotin, P., Tadili, B.-A. & Ramdani, M., 1990. Failles actives dans le Rif central et oriental (Maroc), *C.R. Acad. Sci. Paris*, **310**, 1123–1129.

- Ait Brahim, L., Nakhcha, C., Tadili, B., El Mrabet, A. & Jabour, N., 2004. Structural analysis and interpretation of the surface deformations of the February 24th 2004 Al Hoceima earthquake, *Centre Sismologique Euro-Mediterraneen Newsletter*, **21**, 10–12.
- Backus, G. & Gilbert, F., 1970. Uniqueness in resolving power of gross earth data, *Phil. Trans. R. Soc. Lond., A*, **266**, 123–192.
- Berberian, M., Jackson, J.A., Qorashi, M., Khatib, M.M., Priestley, K., Talebian, M. & Ghafuri-Ashtiani, M., 1999. The 1997 May 10 Zirkuh (Qa'emat) earthquake ( $M_w 7.2$ ): faulting along the Sistan suture zone of eastern Iran, *Geophys. J. Int.*, **136**, 671–694.
- Bezzeghoud, M. & Buforn, E., 1999. Source Parameters of the 1992 Melilla (Spain,  $M_w = 4.8$ ), 1994 Al Hoceima (Morocco,  $M_w = 5.8$ ) and 1994 Mascara (Algeria,  $M_w 5.7$ ) Earthquakes and Seismotectonic Implications, *Bull. seism. Soc. Am.*, **89**, 359–372.
- Bro, R. & De Jong, S., 1997. A fast non-negativity-constrained least squares algorithm, *J. Chemom.*, **11**, 392–401.
- Calais, E., DeMets, C. & Noquet, J.-M., 2003. Evidence for post-3.16-Ma change in Nubia-Eurasia-North America plate motions, *Earth planet. Sci. Lett.*, **216**, 81–92.
- Calvert, A., Gomez, F., Seber, D., Barazangi, M., Jabour, N., Ibenbrahim, A. & Demnati, A., 1997. An integrated geophysical investigation of recent seismicity in the Al-Hoceima Region of North Morocco, *Bull. seism. Soc. Am.*, **87**, 637–651.
- Cherkaoui, T.-E. & Harnafi, M., 2004. Le Seisme d'al Hoceima du 24 Fevrier 2004: Rapport preliminaire de mission du 3 au 7 mars 2004, [http://www.emsc-csem.org/Doc/MOROCCO\\_240204.html](http://www.emsc-csem.org/Doc/MOROCCO_240204.html).
- Das, S. & Scholz, C.H., 1981. Off-fault aftershock clusters caused by shear stress increase? *Bull. seism. Soc. Am.*, **71**, 1669–1675.
- Dillon, W.P., Robb, J.M., Greene, H.G. & Lucena, J.C., 1980. Evolution of the Continental Margin of Southern Spain and the Alboran Sea, *Marine Geology*, **36**, 205–226.
- Du, Y., Aydin, A. & Segall, P., 1992. Comparison of various inversion techniques as applied to the determination of a geophysical deformation model for the 1983 Borah Peak earthquake, *Bull. seism. Soc. Am.*, **82**, 1840–1866.
- Dziewonski, A., Chou, T. & Woodhouse, J., 1981. Determination of earthquake source parameters from waveform data for studies of global and regional seismicity, *J. geophys. Res.*, **86**, 2825–2852.
- El Alami, S.O., Tadilli, B.A., Cherkaoui, T.-E., Medina, F., Ramdani, M., Ait Brahim, L. & Harnafi, M., 1998. The Al Hoceima earthquake of May 26, 1994 and its aftershocks: a seismotectonic study, *Annali di Geofisica*, **41**, 519–537.
- Engdahl, E.R., VanderHilst, R. & Buland, R., 1998. Global teleseismic earthquake relocation with improved travel times and procedures for depth determination, *Bull. Seism. Soc. Am.*, **88**(3), 722–743.
- Fukahata, Y., Nishitani, A. & Matsu'ura, M., 2004. Geodetic Data inversion using ABIC to estimate slip history during one earthquake cycle with viscoelastic slip-response functions, *Geophys. J. Int.*, **156**, 140–153.
- Funning, G.J., 2005. Source Parameters of Large Shallow Earthquakes in the Alpine-Himalayan belt from InSAR and waveform modelling, *D.Phil Thesis*, University of Oxford.
- Funning, G.J., Barke, R.M.D., S.H., Lamb, Minaya, E., Parsons, B. & Wright, T.J., 2005. The 1998 Aiquile, Bolivia earthquake: a seismically active fault revealed with InSAR, *Earth planet. Sci. Lett.*, **232**, 39–49.
- Gesch, D.B., Muller, J.-P., & Farr, T.G., 2006. The Shuttle Radar Topography Mission—data validation and applications, *Photogrammetric Engineering and Remote Sensing*, **72**(3), 233–235.
- Goldstein, R.M. & Werner, C.L., 1998. Radar interferogram filtering for geophysical applications, *Geophys. Res. Lett.*, **25**(21), 4035–4038.
- Goldstein, R.M., Zebker, H.A. & Werner, C.L., 1988. Satellite radar interferometry: two dimensional phase unwrapping, *Radio Science*, **23**(4), 713–720.
- Hanssen, R.F., 2001, *Radar Interferometry: Data Interpretation and Analysis*, Kluwer Acad., Norwell, Massachusetts.
- Hatzfeld, D., Caillot, V., Cherkaoui, T.-E., Jebli, H. & Medina, F., 1993. Microearthquake seismicity and fault plane solutions around the Nekor strike-slip fault, Morocco, *Earth planet. Sci. Lett.*, **120**, 31–34.

- Hudnut, K.W., Seeber, L. & Pacheco, J., 1989. Cross-fault triggering in the November 1987 Superstition Hills earthquake sequence, Southern California, *Geophys. Res. Lett.*, **16**, 199–202.
- Jonsson, S., Zebker, H., Segall, P. & Amelung, F., 2002. Fault slip distribution of the  $M_w$  7.2 Hector Mine earthquake estimated from satellite radar and GPS measurements, *Bull. seism. Soc. Am.*, **92**, 1377–1389.
- Jordan, T.H. & Sverdrup, K.A., 1981. Teleseismic location techniques and their application to earthquake clusters in south-central Pacific, *Bull. seism. Soc. Am.*, **71**, 1105–1130.
- Julian, B., Miller, A. & Foulger, G., 1998. Determination of earthquake source parameters from waveform data for studies of global and regional seismicity, *Rev. Geophys.*, **36**(4), 525–549.
- Kennett, B.L.N., Engdahl, E.R. & Buland, R., 1995. Constraints on seismic velocities in the earth from travel times, *Geophys. J. Int.*, **122**, 108–124.
- Leblanc, D. & Olivier, Ph., 1984. Role of strike-slip faults in the Betic-Rifian Orogeny, *Tectonophysics*, **101**, 345–355.
- Lohman, R.B., Simons, M. & Savage, B., 2002. Location and mechanism of the Little Skull Mountain earthquake as constrained by satellite radar interferometry and seismic waveform modelling, *J. geophys. Res.*, **107**, doi:10.1029/2001JB000627.
- Lohman, R.B. & Simons, M., 2005. Some thoughts on the use of InSAR data to constrain models of surface deformation, *Geochem. Geophys. Geosyst.*, **6**, doi:10.1029/2004GC000841.
- Maggi, A., Jackson, J., Priestley, K. & Baker, C., 2000. A re-assessment of focal depth distributions in southern Iran, the Tien Shan and northern India: do earthquakes really occur in the continental mantle? *Geophys. J. Int.*, **143**, 629–661.
- McCaffrey, R. & Abers, G., 1988. SYN3: A program for inversion of teleseismic body waveforms on microcomputers, *Air Force Geophysics Laboratory Technical Report AFGL-TR-0099*, Hanscomb Air Force Base, Massachusetts.
- McCaffrey, R., Zwick, P. & Abers, G., 1991. SYN4 Program, *IASPEI Software Library*, **4**.
- McClusky, S., Reilinger, R., Mahmoud, S., Ben Sari, D. & Tealeb, A., 2003. GPS constraints on Africa (Nubia) and Arabia plate motions, *Geophys. J. Int.*, **155**, 126–138.
- Meghraoui, M., Morel, J.-L., Andieux, J. & Dahmani, M., 1996. Tectonique Plio-Quaternaire de la chaîne tello-riffaine et de la mer d'Alboran. Une zone complexe de convergence continent-continent, *Bull. Soc. Geol. Fr.*, **167**, 141–157.
- Meghraoui, M., Maouche, S., Chema, B., Cakir, Z., Aoudia, A. & Harbi, A., 2004. Coastal uplift and thrust faulting associated with the  $M_w = 6.8$  Zemmouri (Algeria) earthquake of 21 May, 2003, *Geophys. Res. Lett.*, **31**, doi:10.1029/2004GL020466.
- Menke, W., 1989, *Geophysical Data Analysis: Discrete Inverse Theory*, San Diego: Academic Press.
- Milkereit, C., Gresser, H., Wang, R., Wetzel, H.-U., Woith, H., Karakisa, S., Zunbul, S. & Zschau, J., 2004. Implications of the 2003 Bingöl Earthquake for the Interaction between the North and East Anatolian Faults, *Bull. seism. Soc. Am.*, **94**, 2400–2406.
- Molnar, P. & Lyon-Caen, H., 1989. Fault plane solutions of earthquakes and active tectonics of the Tibetan Plateau and its margins, *Geophys. J. Int.*, **99**, 123–153.
- Morley, C.K., 1987. Origin of a major cross-element zone: Moroccan Rif, *Geology*, **15**, 761–764.
- Nabelek, J., 1984, Determination of earthquake source parameters from inversion of body waves, *PhD thesis*. MIT, Cambridge, Massachusetts.
- Okada, Y., 1985. Surface Deformation due to shear and tensile faults in a half-space, *Bull. seism. Soc. Am.*, **75**, 1135–1154.
- Parsons, B.E., Wright, T.J., Rowe, P., Andrews, J., Jackson, J.A., Walker, R., Khatib, M.M. & Talebian, M., 2006. The 1994 Sefidabeh (eastern Iran) earthquakes revisited: new evidence from satellite radar interferometry and carbonate dating about the growth of an active fold above a blind thrust fault, *Geophys. J. Int.*, **164**, 202–217.
- Robinson, D.P., Henry, C., Das, S. & Woodhouse, J.H., 2001. Simultaneous rupture along two conjugate planes of the Wharton Basin Earthquake, *Science*, **292**, 1145–1148.
- Rosen, P.A., Hensley, S., Peltzer, G. & Simons, M., 2004. Updated Repeat Orbit Interferometry package released, *EOS, Trans. Am. geophys. Un.*, **85**, 35.
- Scholz, C., 1990, *The Mechanics of Earthquakes and Faulting*, Cambridge University Press, Cambridge.
- Simons, M., Fialko, Y. & Rivera, L., 2002. Coseismic Deformation from the 1999  $M_w$  7.1 Hector Mine, California, Earthquake as Inferred from InSAR and GPS Observations, *Bull. seism. Soc. Am.*, **92**, 1390–1402.
- Sipkin, S., 1982. Estimation of earthquake source parameters by the inversion of waveform data: Synthetic waveforms, *Phys. Earth planet. Inter.*, **30**(2–3), 242–259.
- Sipkin, S., 1986a. Estimation of earthquake source parameters by the inversion of waveform data: global seismicity, 1981–1983, *Bull. seism. Soc. Am.*, **76**(6), 1515–1541.
- Sipkin, S., 1986b. Interpretation of non-double-couple earthquake mechanisms derived from moment tensor inversion, *J. geophys. Res.*, **91**(1), 531–547.
- Stein, R.S., 1999. The role of stress transfer in earthquake occurrence, *Nature*, **402**, 605–609.
- Stich, D., Mancilla, F., Baumont, D. & Morales, J., 2005. Source analysis of the  $M_w$  6.3 2004 Al Hoceima earthquake (Morocco) using regional apparent source time functions, *J. geophys. Res.*, **110**(B06306) doi:10.1029/2004JB003366.
- Tsuji, H., Hatanaka, Y., Sagiya, T. & Hashimoto, M., 1995. Coseismic crustal deformation from the 1994 Hokkaido-Toho-Oki earthquake monitored by a nationwide continuous GPS array in Japan, *Geophys. Res. Lett.*, **22**, 1669–1672.
- Walker, R., Jackson, J. & Baker, C., 2004. Active faulting and seismicity of the Dasht-e-Bayaz region, eastern Iran, *Geophys. J. Int.*, **157**, 265–282.
- Wright, T.J., Parsons, B., Jackson, J., Haynes, M., Fielding, E., England, P. & Clarke, P., 1999. Source Parameters of the 1 October 1995 Dinar (Turkey) earthquake from SAR interferometry and seismic bodywave modelling, *Earth planet. Sci. Lett.*, **172**, 23–37.
- Wright, T.J., Lu, Z. & Wicks, C., 2003. Source model for the  $M_w$  6.7 23 October 2002 Nenana Mountain Earthquake (Alaska) from InSAR, *Geophys. Res. Lett.*, **30**, doi:10.1029/2003GL018014.
- Yabuki, T. & Matsu'ura, M., 1992. Geodetic Data Inversion using a Bayesian information criterion for spatial distribution of fault slip, *Geophys. J. Int.*, **109**, 363–375.
- Yielding, G., Jackson, J.A., King, G.C.P., Sinval, H., Vita-Finzi, C. & Wood, W.M., 1981. Relations between surface deformation, fault geometry, seismicity, and rupture characteristics during the El Asnam (Algeria) earthquake of 10 October 1980, *Earth planet. Sci. Lett.*, **56**, 287–304.
- Zwick, P., McCaffrey, R. & Abers, G., 1994. MT5 Program, *IASPEI Software Library*, **4**.